JOURNAL OF THERMOPHYSICS AND HEAT TRANSFER
Vol. 23, No. 4, October–December 2009

Lattice Boltzmann Simulation of Surface Impingement at High-Density Ratio

Xin Gu,* Amit Gupta,* and Ranganathan Kumar†
University of Central Florida, Orlando, Florida 32816

DOI: 10.2514/1.44032

In this work, a novel two-phase lattice Boltzmann method has been employed to study droplet impact dynamics in the presence of a surrounding lighter phase. All the simulations were conducted in a three-dimensional Cartesian coordinate system, with the density ratio of the liquid phase to the gas phase fixed at 50. First, simulations of binary droplet collisions are conducted to validate the methodology for $20 < We < 80$. Three different types of outcome, namely, coalescence collision, separating collision, and stretching collision, are presented. Secondly, the normal impact of a liquid drop impinging on a perfectly smooth dry surface is simulated at various liquid Weber and Reynolds numbers. Results are shown to compare the spread factor dependence on impact velocity, liquid density, liquid viscosity, surface tension, and surface wetting characteristics. The results are validated with experimental data. Two different outcomes are obtained: deposition and splashing breakup. The transition to splashing is found to be dependent on the liquid Weber and Reynolds numbers.

Nomenclature

a, b, T	=	free parameters determining ϕ
B	=	impact parameter
D	=	diameter of the droplet
d	=	diameter of the liquid lamella
E_i, F_i, H_i	=	coefficients in equilibrium distribution functions
$\mathbf{e}_i$	=	particle velocity
f_i	=	particle distribution function for an order parameter
f_i^{eq}	=	equilibrium particle distribution function for f_i
g_i	=	particle distribution function for predicted velocity $\mathbf{u}^*$
g_i^{eq}	=	equilibrium particle distribution function for g_i
h	=	height of the liquid lamella
h_i	=	particle distribution function for pressure
L_x, L_y, L_z	=	dimensions of the computational domain
Oh	=	Ohnesorge number
p	=	pressure
p_0	=	equation of state function determining ϕ
Re	=	Reynolds number
t	=	time in LBM unit
t^*	=	dimensionless time defined as tV/D
$\mathbf{u}$	=	corrected velocity of a two-phase fluid
$\mathbf{u}^*$	=	predicted velocity of a two-phase fluid
V	=	impact velocity
We	=	Weber number
X	=	vertical distance between the centers of the two droplets
Δt	=	time step
Δx	=	lattice spacing
$\delta_{\alpha\beta}$	=	Kronecker delta
ε	=	convergence criteria
η	=	surface wetting force
θ_w	=	static contact angle
κ_f	=	constant parameter determining the width of interface
κ_g	=	constant parameter determining the strength of surface tension
μ	=	viscosity
ξ	=	direction normal to the interface
$\xi_{\max}$	=	maximum spread factor
ρ	=	density
$\bar{\rho}$	=	averaged density
σ	=	surface tension
τ_f	=	relaxation time for f_i
τ_g	=	relaxation time for g_i
τ_h	=	relaxation time for h_i
ϕ	=	order parameter to distinguish two phases
ψ	=	bulk free-energy density
Ω	=	wetting potential
Ω_i	=	collision operator

Subscripts

G	=	gas phase
L	=	liquid phase
α, β, γ	=	Cartesian coordinates

I. Introduction

THE collision of droplet(s) on solid or liquid surfaces is a phenomenon that occurs widely in nature. Impact of drops on solid surfaces is a very common phenomenon in many modern engineering applications ranging from ink-jet printing to spray cooling, internal combustion engines to spray painting and plasma spraying, and more recently in microfabrication and microchannels [1]. Experimental investigations have been carried out extensively to study the mechanism of droplet impact and the subsequent spreading process on a dry/wet surface [2–4]. These have been directed toward studying the heat transfer to a droplet that falls on a dry hot surface [2] and subsequently breaks off into daughter drops, droplet spreading behavior on a rough surface and the formation of a water sheet [3], and impact of a single drop on a thin liquid film to delineate the parameter range for which the drop can deposit on the film, or splash forming a crownlike structure which grows with time and may lead to subsequent pinch-off of a small secondary droplet from the rim of the crown [4]. Numerical investigations of a droplet splashing phenomenon have primarily been focused toward impact dynamics on a wet surface with a variable thickness of the liquid layer [5–9].

Presented as Paper 1249 at the 47th AIAA Aerospace Sciences Meeting, Orlando, FL, 5–8 January 2009; received 25 February 2009; accepted for publication 4 June 2009.

*Graduate Student, Department of Mechanical, Materials and Aerospace Engineering, 4000 Central Florida Boulevard.

†Professor, Department of Mechanical, Materials and Aerospace Engineering, 4000 Central Florida Boulevard; rnkumar@mail.ucf.edu (Corresponding Author).

These simulations have been conducted using the volume-of-fluid method [5,6], an axisymmetric lattice Boltzmann model for high-density ratios [7,8] and a high-density lattice Boltzmann model with a planar–cylinder impact on a thin film of liquid [9].

However, numerical simulations of multiphase flows are a very challenging class of problems because of the inherent difficulty in tracking the fluid interfaces, mass conservation, and the correct treatment of the surface tension force. In recent years, the lattice Boltzmann method (LBM) has emerged as a very promising numerical approach for simulation of complex and multiphase flows. The success of LBM based simulations is mainly due to their mesoscopic and kinetic nature, which enables the simulation of macroscopic interfacial dynamics with the underlying microscopic nature. Gunstensen et al. [10] were the first to develop a multi-component LBM based on the two-component lattice gas model. Shan and Chen [11] proposed an LBM model using microscopic interactions for multiphase fluid flows, better known as the pseudopotential method. Swift et al. [12] developed a multiphase LBM model based on the free-energy approach. He et al. [13] also proposed a new variant of the multiphase LBM model using the kinetic equation for multiphase flows. However, all of the previous schemes are limited to small density ratios of less than 10 and suffer from instability when dealing with larger density ratios. Inamuro et al. [14] first proposed an LBM scheme which was able to deal with such two-phase fluid flows of density ratio up to 1000. More recently, Lee and Lin [9] devised a new LBM scheme which enables stable simulation of two-phase flows with high-density and viscosity ratios. However, they reported that their method introduces anisotropy due to special treatment of discretization of forcing terms in the lattice Boltzmann equation.

So far, there have been a few studies dealing with liquid–wall interaction using LBM [15–19]. These studies have separately validated their method by using Young's equation, according to which the static contact angle between the liquid–gas interface and the wall is an outcome of the interfacial tension forces between the three phases: liquid, gas, and solid. However, there are only two prior studies of droplet impact on a dry surface using LBM. The first one, by Mukherjee and Abraham [20], employed an axisymmetric LBM model to study the impact of a droplet on a wall within a density ratio of 10. They found that a droplet impinging on a super hydrophobic surface may completely lift off from the surface, leading to a rebound. In a recent work, Gupta and Kumar [21] systematically studied the droplet spreading diameter at various Weber and Reynolds numbers by using the pseudopotential model. They found that under certain conditions, a droplet impinging on a nonwetting surface may result in an in-plane breakup of the spreading film. Again, their simulations were done within a density ratio of 10. In this present study, a relatively high-density ratio of 50 will be used for the simulations.

II. Methodology: Lattice Boltzmann Equation

A. Basic Lattice Boltzmann Equation: An Extension of Lattice Gas Automata

The lattice Boltzmann equation is derived from its earlier remnant, called the lattice gas automata, in which a simple discrete kinetic equation describes the evolution of a particle distribution function:

$$f_i(\mathbf{x}+\mathbf{e}_i\Delta t, t+\Delta t) = f_i(\mathbf{x},t) + \Omega_i(f_i(\mathbf{x},t)) \quad (i=0,1,2\ldots,M) \tag{1}$$

where f_i is the single particle distribution function along the ith direction, which describes the probability that a particle will appear in an infinitesimal region of phase space around $\mathbf{x}$, with speed $\mathbf{e}_i$ at time t. Ω_i is the collision operator representing the rate of change of particle distribution due to collision. We have used the particular form of the collision operator with the single time relaxation approximation, also known as the lattice Bhatnagar–Gross–Krook operator:

$$\Omega_i(f_i(\mathbf{x},t)) = -\frac{f_i(\mathbf{x},t) - f_i^{\mathrm{eq}}(\mathbf{x},t)}{\tau} \tag{2}$$

where f_i^{eq} is the equilibrium distribution function at (x,t), and τ is the rate at which the local particle distribution relaxes to an equilibrium state, given as

$$f_i^{\mathrm{eq}} = \omega_i\rho\left[1 + \frac{\vec{\mathbf{e}}_i\cdot\vec{\mathbf{u}}}{c_s^2} + \frac{(\vec{\mathbf{e}}_i\cdot\vec{\mathbf{u}})^2}{2c_s^2} + \frac{\vec{\mathbf{u}}\cdot\vec{\mathbf{u}}}{2c_s^2}\right] \tag{3}$$

where $\omega_i = 4/9$ for $i=0$; $\omega_i = 1/9$ for $i=1,2,3,$ and 4; $\omega_i = 1/36$ for $i=5,6,7,$ and 8 for a two-dimensional, nine-speed phase-space discretization. c_s is the speed of sound in lattice units, and is given by $c_s^2 = 1/3$.

Thus, the LBM evolution step can be summarized into two steps: the collision step and the streaming step:

$$\text{Collision: } f_i^c(\mathbf{x}, t+\Delta t) = f_i(\mathbf{x},t) + \Omega_i(\mathbf{x},t)$$
$$\text{Streaming: } f_i(\mathbf{x}+\mathbf{e}_i\Delta t, t+\Delta t) = f_i^c(\mathbf{x}, t+\Delta t) \tag{4}$$

where superscript c denotes postcollision quantity.

In the discrete lattice space, the macroscopic density per node $\rho(\mathbf{x},t)$ and the macroscopic velocity $\mathbf{u}(\mathbf{x},t)$ are defined in terms of the particle distribution functions as

$$\rho(\mathbf{x},t) = \sum_i f_i(\mathbf{x},t) = \sum_i f_i^{\mathrm{eq}}(\mathbf{x},t) \tag{5a}$$

$$\mathbf{u}(\mathbf{x},t) = \sum_i \mathbf{e}_i f_i(\mathbf{x},t)/\rho(\mathbf{x},t) \tag{5b}$$

In the limit that the Knudsen number is small, that is, $Kn \ll 1$, the Chapman–Enskog expansion reduces this microscopic LBM formulation into the macroscopic Navier–Stokes equation in the nearly incompressible limit:

$$\frac{\partial\rho}{\partial t} + \nabla\cdot(\rho\vec{\mathbf{u}}) = 0 \tag{6a}$$

$$\rho\left(\frac{\partial\mathbf{u}_\alpha}{\partial t} + \nabla_\beta\cdot\mathbf{u}_\alpha\mathbf{u}_\beta\right) = -\nabla_\alpha p + \upsilon\nabla_\beta\cdot(\nabla_\alpha\rho\mathbf{u}_\beta + \nabla_\beta\rho\mathbf{u}_\alpha) \tag{6b}$$

where p is the pressure and υ is the kinematic viscosity, which is given as follows:

$$p = c_s^2\rho = \rho/3 \quad \text{and} \quad \upsilon = (2\tau-1)/6$$

B. Two-Phase Lattice Boltzmann Model

In this study, the 15-velocity model for three-dimensions (D3Q15) as used by Inamuro et al. [14] has been implemented. The velocity vectors in this model are given by (see Fig. 1)

$$[e_1,e_2,e_3,e_4,e_5,e_6,e_7,e_8,e_9,e_{10},e_{11},e_{12},e_{13},e_{14},e_{15}] = \begin{bmatrix} 0 & 1 & 0 & 0 & -1 & 0 & 0 & 1 & -1 & 1 & 1 & -1 & 1 & -1 & -1 \\ 0 & 0 & 1 & 0 & 0 & -1 & 0 & 1 & 1 & -1 & 1 & -1 & -1 & 1 & -1 \\ 0 & 0 & 0 & 1 & 0 & 0 & -1 & 1 & 1 & 1 & -1 & -1 & -1 & -1 & 1 \end{bmatrix} \tag{7}$$

In the present method, two-phase fluid flow simulations have been carried out for a purely isothermal system. Two particle distribution functions f_i and g_i have been introduced. Function f_i is used to calculate the order parameter ϕ, which distinguishes the two phases, while g_i is used to calculate a predicted velocity $\mathbf{u}^*$ of the two-phase fluids without a pressure gradient. The evolution of the particle distribution functions $f_i(\mathbf{x},t)$ and $g_i(\mathbf{x},t)$ with particle velocity $\mathbf{e}_i$ at the point $\mathbf{x}$ and time t is carried out by the following equations:

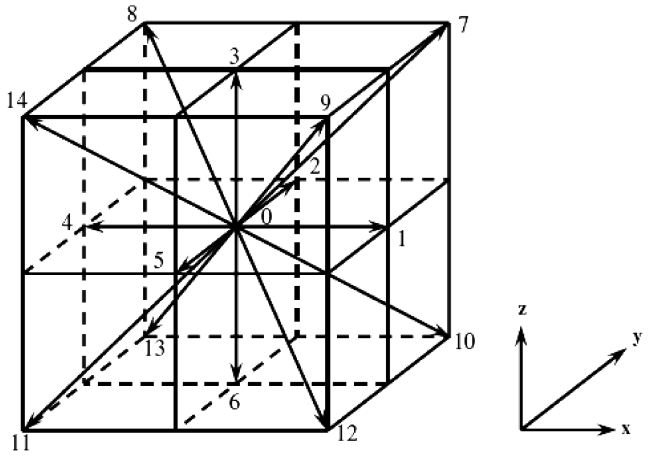

Fig. 1 Discrete velocity vectors for the D3Q15 lattice Boltzmann model.

$$f_i(\mathbf{x}+\mathbf{e}_i\Delta t, t+\Delta t) = f_i(\mathbf{x},t) - \frac{f_i(\mathbf{x},t) - f_i^{\mathrm{eq}}(\mathbf{x},t)}{\tau_f} \tag{8}$$

$$g_i(\mathbf{x}+\mathbf{e}_i\Delta t, t+\Delta t) = g_i(\mathbf{x},t) - \frac{g_i(\mathbf{x},t) - g_i^{\mathrm{eq}}(\mathbf{x},t)}{\tau_g} + 3E_i\mathbf{e}_{i\alpha}\frac{1}{\rho}\left[\frac{\partial}{\partial x_\beta}\left\{\mu\left(\frac{\partial \mathbf{u}_\beta}{\partial x_\alpha}+\frac{\partial \mathbf{u}_\alpha}{\partial x_\beta}\right)\right\}\right]\Delta x \tag{9}$$

The last term in Eq. (9) represents the viscous stress tensor. f_i^{eq} and g_i^{eq} are the modified particle equilibrium distributions for this heuristic two-phase model chosen to satisfy the desired evolution equations as shown next.

The macroscopic variables, order parameter ϕ, and the predicted velocity of two-phase fluids $\mathbf{u}^*$ are given from the moments of the functions f_i and g_i at each location, and are given as

$$\phi = \sum_{i=1}^{15} f_i \tag{10}$$

$$\mathbf{u}^* = \sum_{i=1}^{15} \mathbf{e}_i g_i \tag{11}$$

The equilibrium functions f_i^{eq} and g_i^{eq} are given by

$$f_i^{\mathrm{eq}} = H_i\phi + F_i\left[p_0 - \kappa_f\phi\frac{\partial^2\phi}{\partial x_\alpha^2} - \frac{\kappa_f}{6}\left(\frac{\partial\phi}{\partial x_\alpha}\right)^2\right] + 3E_i\phi e_{i\alpha}u_\alpha + E_i\kappa_f G_{\alpha\beta}(\phi)e_{i\alpha}e_{i\beta} \tag{12}$$

$$g_i^{\mathrm{eq}} = E_i\left[1 + 3e_{i\alpha}u_\alpha - \frac{3}{2}u_\alpha u_\alpha + \frac{9}{2}e_{i\alpha}e_{i\beta}u_\alpha u_\beta + \frac{3}{2}\left(\tau_g - \frac{1}{2}\right)\left(\frac{\partial u_\beta}{\partial x_\alpha}+\frac{\partial u_\alpha}{\partial x_\beta}\right)e_{i\alpha}e_{i\beta}\right] + E_i\frac{\kappa_g}{\rho}G_{\alpha\beta}(\rho)e_{i\alpha}e_{i\beta} - \frac{2}{3}F_i\frac{\kappa_g}{\rho}\left(\frac{\partial\rho}{\partial x_\alpha}\right)^2 \tag{13}$$

where

$$E_i = \begin{cases} 2/9, & i=1, \\ 1/9, & i=1,\ldots,7 \\ 1/72, & i=8,\ldots,15 \end{cases}$$

$$F_i = \begin{cases} -7/3, & i=1, \\ 1/3, & i=1,\ldots,7, \\ 1/24, & i=8,\ldots,15, \end{cases} \qquad H_i = \begin{cases} 1, & i=1, \\ 0, & i=1,\ldots,15 \end{cases} \tag{14}$$

and

$$G_{\alpha\beta}(\phi) = \frac{9}{2}\frac{\partial\phi}{\partial x_\alpha}\frac{\partial\phi}{\partial x_\beta} - \frac{3}{2}\frac{\partial\phi}{\partial x_\gamma}\frac{\partial\phi}{\partial x_\gamma}\delta_{\alpha\beta} \tag{15}$$

and p_0 is the thermodynamic pressure, given by

$$p_0 = \phi\frac{\partial\psi}{\partial\phi} - \psi = \phi T\frac{1}{1-b\phi} - a\phi^2 \tag{16}$$

with

$$\psi(\phi,T) = \phi T In\left(\frac{\phi}{1-b\phi}\right) - a\phi^2 \tag{17}$$

The first derivatives and laplacian operators ($\partial\phi/\partial x_\alpha$, $\partial\rho/\partial x_\alpha$, $\partial u_\beta/\partial x_\alpha$, $\nabla^2\phi$, and $\nabla^2 u_\alpha$) are calculated using the finite difference approximations in the lattice Boltzmann construction and involves the effects from all neighboring nodes, given as

$$\frac{\partial\lambda}{\partial x_\alpha} \approx \frac{1}{10}\sum_{i=2}^{15} e_{i\alpha}\lambda(\mathbf{x}+\mathbf{e}_i\delta t) \tag{18}$$

$$\nabla^2\lambda \approx \frac{1}{5}\left[\sum_{i=2}^{15}\lambda(\mathbf{x}+\mathbf{e}_i\delta t) - 14\lambda(x)\right] \tag{19}$$

Once the order parameter is determined from the zeroth order moment of the distribution function f_i, the density at the interface is then calculated by

$$\rho = \begin{cases} \rho_G & \phi < \phi_G^* \\ \frac{\Delta\rho}{2}[\sin(\frac{\phi-\bar{\phi}^*}{\Delta\phi^*}\pi)+1] + \rho_G & \phi_G^* \le \phi \le \phi_L^* \\ \rho_L & \phi > \phi_L^* \end{cases} \tag{20}$$

where $\Delta\rho = \rho_L - \rho_G$, $\Delta\phi^* = \phi_L^* - \phi_G^*$, and $\bar{\phi}^* = (\phi_L^* + \phi_G^*)/2$. It is important to introduce the cutoff values of the order parameters ϕ_L^* and ϕ_G^* as the maximum and minimum values of the order parameter ϕ are found to deviate a little from their initial values during the course of the simulation. These cutoff values help to keep the density of each phase at constant values during the entire simulation duration.

The dynamic viscosity for the two phases across the interface is computed based on a linear interpolation as

$$\mu = \frac{\rho-\rho_G}{\rho_L-\rho_G}(\mu_L-\mu_G) + \mu_G \tag{21}$$

The surface tension σ between the liquid and gas phases is given by

$$\sigma = \kappa_g\int_{-\infty}^{\infty}\left(\frac{\partial\rho}{\partial\xi}\right)^2 \mathrm{d}\xi \tag{22}$$

In all the simulations carried out in the present paper, the surface tension σ is calculated as a postprocessing value after conducting static droplet tests. σ is numerically integrated along the interface after the two phases have been equilibrated. The predicted velocity given by $\mathbf{u}^*$ is not divergence free, because it is derived based on a flow without a pressure gradient. To acquire the correct velocity field, the following corrections are incorporated:

$$\mathbf{u} - \mathbf{u}^* = -\frac{\nabla p}{\rho} \tag{23}$$

$$\nabla\cdot\left(\frac{\nabla p}{\rho}\right) = \nabla\cdot\mathbf{u}^* \tag{24}$$

where p is the pressure of the two-phase fluid, which is obtained by solving Eq. (25) in the following LBM framework:

$$h_i^{n+1}(\mathbf{x}+\mathbf{e}_i\Delta t) = h_i^n(\mathbf{x}) - \frac{1}{\tau_h}[h_i^n(\mathbf{x}) - E_i p^n(\mathbf{x})] - \frac{1}{3}E_i\frac{\partial \mathbf{u}_\alpha^*}{\partial x_\alpha}\Delta x \tag{25}$$

where the superscript n represents the number of iterations and $\tau_h = \frac{1}{\rho} + \frac{1}{2}$ is the relaxation time for particle distribution function h_i used to update the pressure field. The moment of the distribution function h_i yields the pressure field as

$$p = \sum_{i=1}^{15} h_i \tag{26}$$

The system of Eqs. (23–26) is solved until the following convergence criteria is satisfied:

$$|p^{n+1} - p^n|/\rho < \varepsilon \tag{27}$$

C. Novel Treatment for the Wetting Boundary Condition

When a liquid–gas interface meets a solid surface, an angle is formed between the interface and the surface. This angle, which is measured in the liquid, is called the static contact angle, θ_w. According to Young's equation:

$$\cos\theta_w = \frac{\sigma_{sg} - \sigma_{sl}}{\sigma} \tag{28}$$

where σ_{sg} is the surface tension force between solid and gas, and σ_{sl} is the surface tension force between solid and liquid.

Recently, a novel LBM boundary condition was proposed by Briant et al. [15] which enabled the static contact angle between the liquid–gas interface and the wall to be controlled in a way that is consistent with the Cahn theory [22]. In their method, the required wetting potential Ω was calculated by choosing a desired wetting property of the solid surface (i.e., the wetting angle θ_w). Then, the derivative of density normal to the wall, $\partial\rho/\partial n$, was evaluated to calculate the equilibrium particle distribution functions on the wall. By following such a process, the effect of the (input) wall wetting characteristics could be transmitted to the interior fluid nodes through the equilibrium particle distribution functions. Their static droplet simulations showed that the input and postprocessed contact angles match accurately.

In the present work, a treatment of the wall boundary condition similar to Briant's work has been adopted, but with a minor modification due to a difference in the equation of state. Briant et al. [15] had used a modified van der Waals free-energy function that enables the surface tension force to be an input parameter. In Inamuro et al.'s method [14], the traditional form of the van der Waals free energy was used, and the surface tension was a postprocessed parameter. In lieu of this difference, instead of specifying an input static contact angle θ_w, an input surface wetting force η was used to obtain the equilibrium particle distribution functions on the wall in the current study. Thus, the first and second derivatives of the order parameter can be treated as

$$\left.\frac{\partial\phi}{\partial z}\right|_{z=0} = -\eta \tag{29}$$

$$\left.\frac{\partial^2\phi}{\partial z^2}\right|_{z=0} \approx \frac{1}{2}\left(-3\left.\frac{\partial\phi}{\partial z}\right|_{z=0} + 4\left.\frac{\partial\phi}{\partial z}\right|_{z=1} - \left.\frac{\partial\phi}{\partial z}\right|_{z=2}\right) \tag{30}$$

where z is the direction perpendicular to the wall. Equation (29) was used to calculate the first term on the right-hand side of Eq. (30). The second and third terms were calculated by standard central-difference and backward-difference (taken into the wall) formulas, given by

$$\left.\frac{\partial\phi}{\partial z}\right|_{z=2} \approx \frac{1}{2}(3\phi|_{z=2} - 4\phi|_{z=1} + \phi|_{z=0}) \tag{31}$$

III. Benchmark Tests: Drop Collision Dynamics

In this section, results from the binary droplet collision simulations used to benchmark the numerical methodology are presented. Two liquid droplets with the same diameter D were placed a distance $2D$ apart in the gas phase and were allowed to move toward each other with a relative collision velocity given by V, as shown in Fig. 2. The droplet collision dynamics is described in terms of three important dimensionless parameters, given by

$$\text{Weber number}: We = \frac{\rho_L V^2 D}{\sigma} \tag{32}$$

$$\text{Reynolds number}: Re = \frac{\rho_L V D}{\mu_L} \tag{33}$$

$$\text{Impact parameter}: B = \frac{X}{D} \tag{34}$$

where X is the vertical distance between the centers of the two droplets (see Fig. 2).

For all the simulations presented herein, the density ratio ρ_L/ρ_G is fixed at 50 ($\rho_L = 50$, $\rho_G = 1$). The viscosities of liquid and gas are $\mu_L = 8\times10^{-2}$, $\mu_G = 1.6\times10^{-3}$. The relative velocity is chosen to be $V = 0.1$. The initial diameter of the spherical droplets is $D = 32$. The Reynolds number is fixed at $Re = 2000$ for all the simulations, while the Weber number is varied in the range of $20 < We < 80$ by varying κ_g. Symmetric boundary conditions are employed along the y axis, thereby reducing the computational time in half.

In Fig. 3, the time evolution of the binary droplets after collision is shown for $We = 20$ and $B = 0$. The droplet shape represents the interface where the mean density, given by $\bar{\rho} = (\rho_L + \rho_G)/2 = 25.5$, occurs. It can be observed that the two droplets experience a small deformation as they approach each other ($t^* = 1.56$). The conjoined droplets reach a maximum elongation in the vertical direction z at $t^* = 3.13$. Subsequently, the extent of deformation decreases, as the surface tension force pulls the droplet to recover its spherical shape. However, the momentum gained by the recoiling motion enables the droplet to form a stretched liquid cylinder after having reached its maximum deformation in the x direction

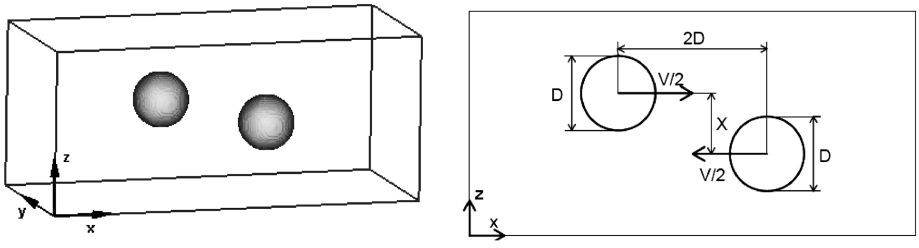

Fig. 2 Computational domain for binary droplet collision.

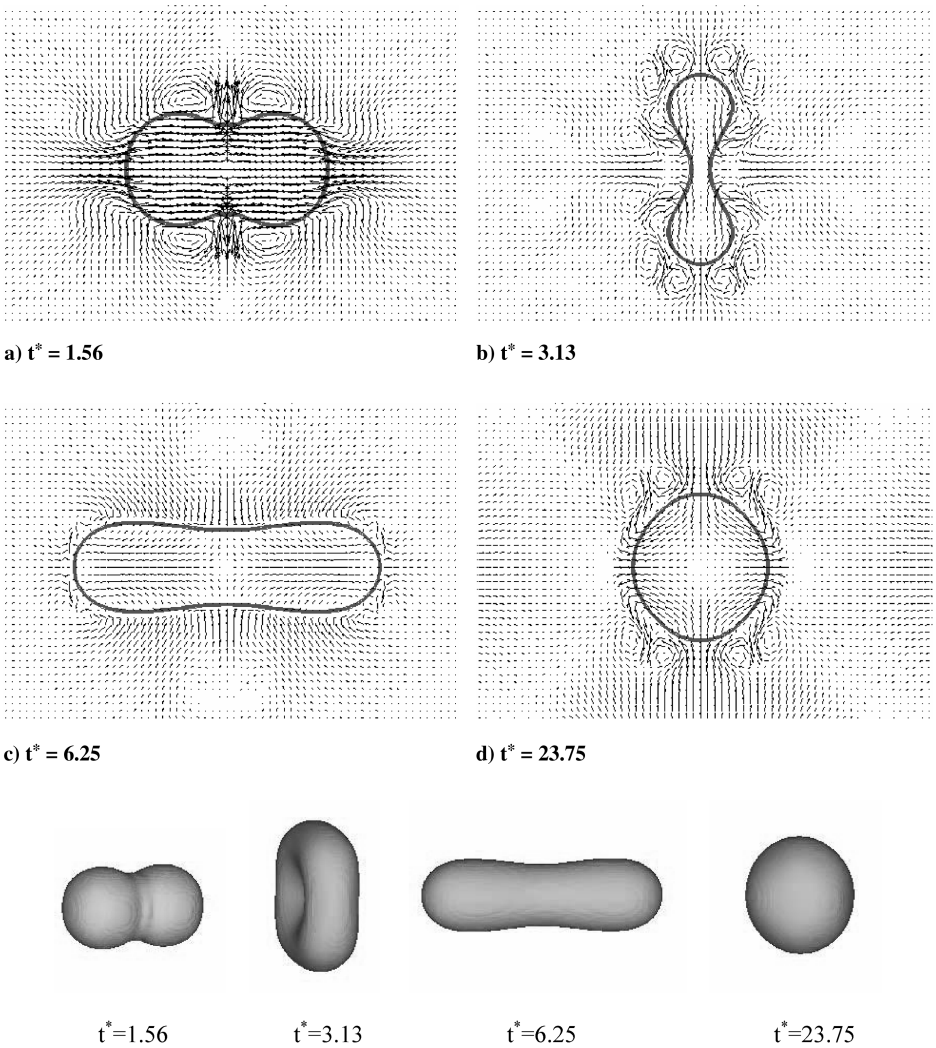

Fig. 3 Evolution of droplet shape with time for $We = 20$ and $B = 0$.

($t^* = 6.25$). After some oscillations, this exchange of surface tension energy and momentum is dissipated completely, and the cylinder transforms into a spherical droplet ($t^* = 23.75$). This class of collisions is called the "coalescence collision."

In Fig. 4, the time evolution of the binary droplets collision mechanism is shown for a slightly higher $We = 40$ and $B = 0$. The droplet interface shown represents $\bar{\rho} = (\rho_L + \rho_G)/2 = 25.5$. The time evolution of the droplet shape is very similar to the case shown in Fig. 3 up to the formation of the long liquid cylinder. However, in this case, the cylinder breaks into two major droplets and a small satellite droplet in the middle ($t^* = 15.0$). This type of collision is called the "reflexive separation collision."

Figure 5 describes the time evolution of the binary droplets collision for a case when $We = 80$ and $B = 0.5$. The two droplets collide at a higher impact parameter, thereby only a small portion of them comes in direct contact with each other. The rest of the conjoint droplet moves with the initial inertia. Eventually, the conjoint droplet breaks into two major droplets with a small satellite droplet. This type of collision is known as a "stretching separation collision."

IV. Droplet Impingement

In this section, results from the normal impact of a liquid droplet onto a solid, dry surface are reported and discussed. The impact is assumed to be isothermal, and the dry surface is assumed to be perfectly smooth. The physical variables that affect such an impact include the initial droplet diameter D, impact velocity V, liquid density ρ_L, viscosity μ_L, liquid–gas interfacial tension σ, and the surface wettability. These variables can be grouped into two important dimensionless numbers, namely, the Weber and the Reynolds numbers. In addition to the Weber and Reynolds numbers, a third parameter has been used in the literature to describe the interplay of viscous and surface tension forces and is known as the Ohnesorge number, given by

$$Oh = \sqrt{We}/Re = \mu_L/\sqrt{\rho_L D\sigma} \tag{35}$$

In addition, the spreading characteristics of this dynamic process are captured by measuring the spreading film diameter. This quantity is usually represented by a dimensionless number known as the spread factor, given as $d^* = d/D$, and is defined as the ratio of spreading film diameter d to the initial spherical droplet diameter D. The evolution time t is made dimensionless using impact velocity V and the initial spherical drop diameter D, as $t^* = tV/D$. The time evolution of the spread factor can be divided into four phases: the kinematic phase, the spreading phase, the relaxation phase, and the wetting/equilibrium phase [23]. Figure 6 shows a typical curve for the time evolution of the spread factor for $We = 36$ and $Re = 200$ and $\theta_w = 66.7$ deg. The spread factor can be observed to acquire a maximum value of 2.1 at the end of the spreading phase.

A. Computational Setup

The three-dimensional computational domain with lengths L_x, L_y, and L_z along the x, y, and z axes, respectively, and its two-dimensional cross section at $y = L_y/2$ are shown in Fig. 7. A periodic boundary condition was used on the sides of the domain (along the x and y

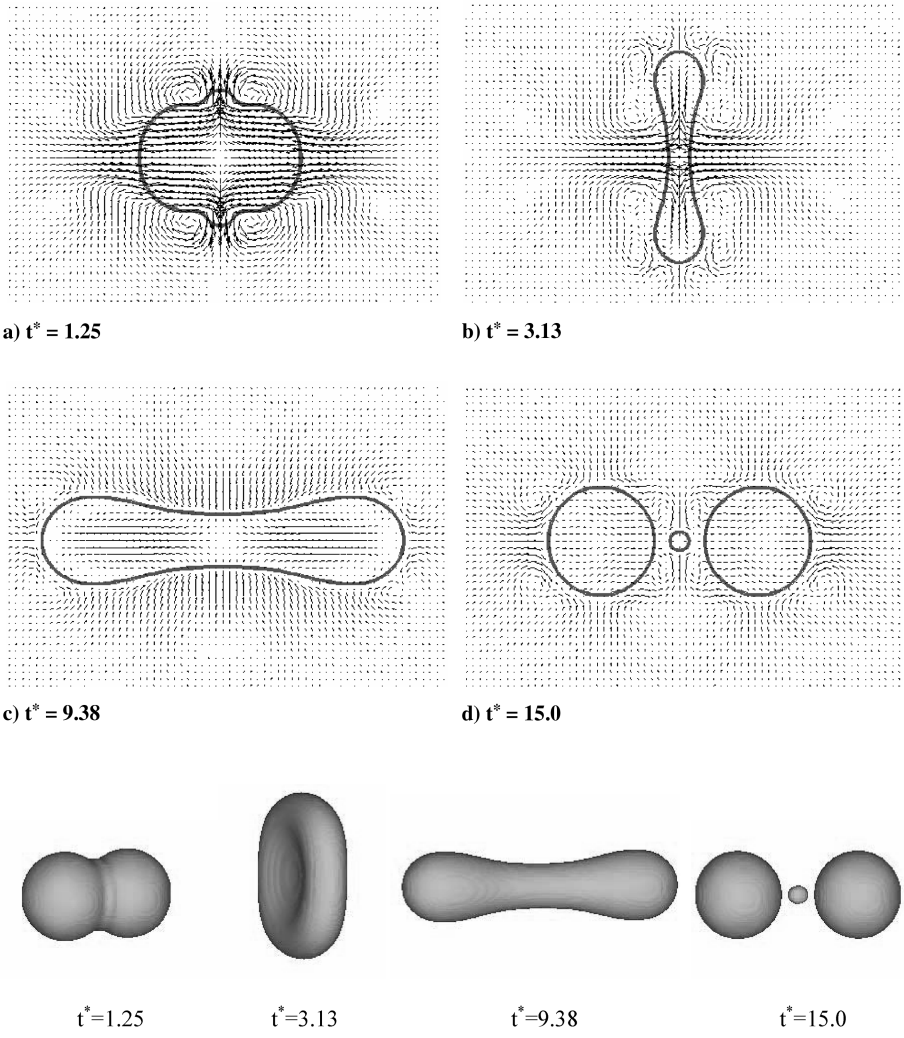

Fig. 4 Evolution of droplet shape with time for $We = 40$ and $B = 0$.

directions), while a no-slip wall boundary condition was used on the top and bottom boundaries of the domain. Using a free slip or open boundary condition for the top boundary of the domain was found to have little effect on the simulation results presented herein. Because of massive computation requirements of a three-dimensional simulation, only one-quarter of the domain is simulated, thereby using symmetry at $x = L_x/2$ and $y = L_y/2$. The domain size for each case was varied according to the initial size of the droplet chosen.

Initially, the droplet was placed several nodes away from the surface and was allowed to equilibrate for 5000 time steps. At this time, the droplet is assigned a uniform velocity V in the vertical direction for about 100 time steps to make sure that the drop attains a steady impact velocity. The viscosity ratio of liquid and gas was fixed at $\mu_L/\mu_G = 50$. The diameter of the droplet was fixed at $D = 32$. For all other parameters: $a = 1$, $b = 6.7$, $T = 0.035$, it follows that $\phi_{\max} = 9.714 \times 10^{-2}$ and $\phi_{\min} = 1.134 \times 10^{-2}$. The cutoff values of the order parameter are $\phi_L^* = 9.2 \times 10^{-2}$ and $\phi_G^* = 1.5 \times 10^{-2}$, $\kappa_f = 0.5$, $\tau_f = 1$, $\tau_g = 1$, and $\varepsilon = 10^{-5}$. The Weber number was varied by changing parameter κ_g, while the Reynolds number was varied by changing liquid viscosity μ_L.

B. Preliminary Wetting Tests

Even before running a droplet impact case, a preliminary wetting test was conducted to obtain the desired surface wetting characteristic, represented by the static contact angle θ_w. As an initial condition, one-half of a spherical droplet was placed at the center of the bottom surface with a specified value for the surface wetting force, depending on whether the surface is hydrophilic, neutral, or hydrophobic. This test was allowed to run for 20,000 time steps to obtain a stable equilibrium state. Figure 8 shows results for such a test with a different wetting behavior, namely, a) a hydrophilic surface, where $\theta_w = 66.7$ deg with $\eta = 3 \times 10^{-3}$, b) a neutral surface, where $\theta_w = 90$ deg with $\eta = 0$, and c) a hydrophobic surface, where $\theta_w = 105$ deg with $\eta = -5 \times 10^{-3}$.

C. Validation of Power Law During Kinematic Phase

Figure 9 shows the droplet shape in the kinematic phase defined for the very early stages of impact. During this phase, the spreading droplet represents a truncated sphere without the formation of a spreading lamella along the surface of the wall. According to the geometry shown in Fig. 9, we can write the following approximated equation:

$$(d/2)^2 = (D/2)^2 - (D/2 - Vt)^2$$
$$\Rightarrow d = 2\sqrt{DVt - (Vt)^2} \Rightarrow d^* = 2\sqrt{t^*(1 - t^*)} \tag{36}$$

For small t^*, that is, $t^* \ll 1$, Eq. (36) indicates that d^* is proportional to $t^{*0.5}$, with an approximate coefficient of 2. Rioboo et al. [23] obtained a coefficient of 2.8 from numerous experimental data. Figure 10 shows a collection of six cases using the current formulation of LBM, with a curve fit of $d^* = 2.5^* t^{*0.5}$, in which the coefficient lies between the theoretical prediction and the experimental data. This validation predicts that the droplet spreading factor in the kinematic phase is only a function of the dimensionless time and does not depend on the physical properties of the fluids involved.

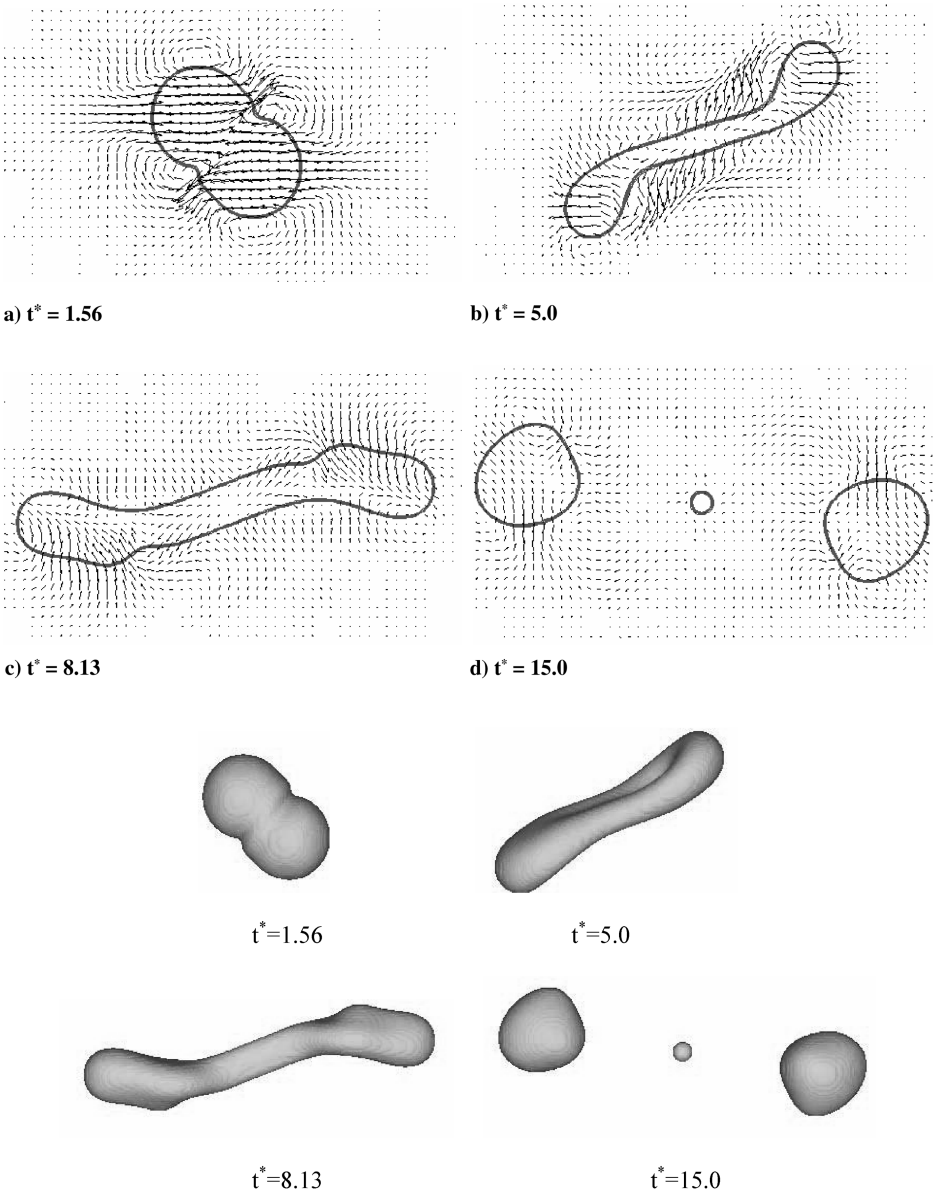

Fig. 5 Evolution of droplet shape with time for $We = 80$ and $B = 0.5$.

D. Simulation Observations

After the kinematic phase, other physical parameters, inertia of impact, and surface tension forces begin to play a role to influence the spread factor and the subsequent droplet deformation process. Figure 11 shows how the droplet deforms with time, and velocity vectors both inside and outside of the droplet are also clearly presented. The Weber number is chosen to be 50, the Reynolds number is chosen to be 1000, and the wall has neutral wetting characteristics. The snapshots are taken at different stages of the spreading lamella to show different regimes of the droplet shape. Figure 11a shows the droplet deformation at an early stage of impact. During this kinematic phase, the bottom of the spherical droplet is highly squeezed to the sides, thereby producing large velocity currents at the edge of the droplet. The formation of a vortex in the gas phase due to movement of the droplet in the downward direction can also be observed. Figure 11b shows that a lamella is formed and bounded by a rim when the droplet continues to spread, which reaches its maximum diameter (see Fig. 11c), indicating the end of the spreading phase. The end of the spreading phase can also be judged by observing the velocity vectors at the edge of the lamella, which almost turn to zero. Figures 11d and 11e show the rest of the spreading process as the lamella begins to recoil back during the relaxation phase and eventually reaches its maximum height (see Fig. 11e). After oscillating for a long time between $t^* = 6.8$ and $t^* = 23.2$, the droplet finally reaches the equilibrium state shown by Fig. 11f, where a half spherical droplet sits on the dry surface. Figure 12 shows the corresponding three-dimensional droplet deformation with time.

E. Maximum Spread Factor Analysis

According to mass conservation of the liquid film before and after impact:

$$\frac{\pi}{6}D^3 \approx \frac{\pi}{4}(Dd_{\max})^2 h \tag{37}$$

where $d_{\max}$ is the maximum spread factor, and h is the height of the lamella when the droplet reaches its maximum spread factor. This yields

$$d_{\max} \approx \sqrt{\frac{2D}{3h}} \tag{38}$$

Because of the diffusive nature of LBM [9,24], the interface thickness between liquid and gas should not be any smaller than 2, otherwise the lamella might diffuse away. Since $D = 32$ is used for

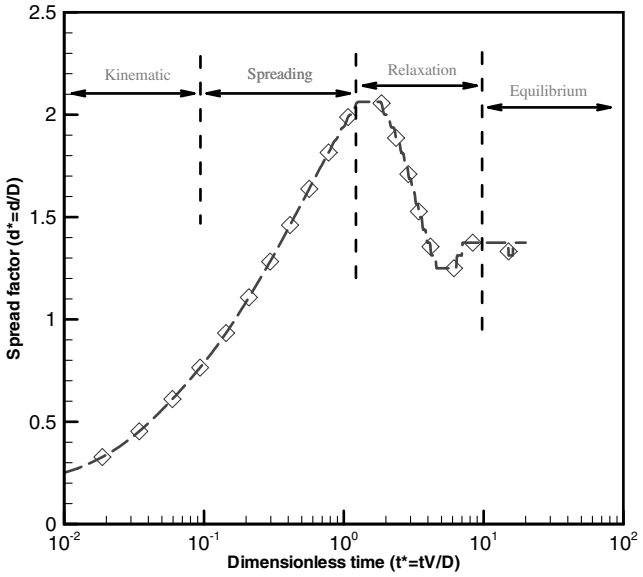

Fig. 6 Time evolution of spread factor showing four distinct phases: kinematic, spreading, relaxation, and equilibrium. Data obtained using 3-D LBM simulation for $We = 36$ and $Re = 200$.

all the simulation cases, and assuming $h \geq 3$, Eq. (38) reduces to $d_{\max} \leq 2.67$. Thus, all the simulations conducted are properly chosen to meet this requirement on the maximum spread factor.

F. Parametric Analysis on the Maximum Spread Factor

In this section, three groups, the surface wettability, the Weber number, and the Reynolds number, are studied separately to examine their influence on the liquid spreading behavior in the spreading phase.

In Fig. 13, three different surfaces have been used: hydrophilic, neutral, and hydrophobic with static contact angles of $\theta_w =$ 66.7 deg, $\theta_w = 90$ deg, and $\theta_w = 105$ deg, respectively. As one can observe from the figure, all three curves behave in a similar fashion during most of the spreading phase. However, after $t^* = 1$, some differences can be seen such as the following: on the hydrophilic surface, the droplet reaches a maximum spread factor of 2.45; on the neutral surface, the droplet reaches a maximum spread factor of 2.15; on the hydrophobic surface, the droplet reaches a maximum spread factor of 2.05. These results show that the surface

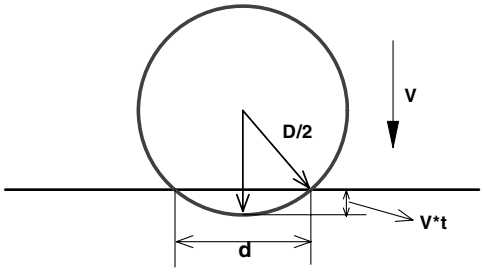

Fig. 9 Early stage of impact-kinematic phase.

wettability does have an influence on the maximum spread factor. Clearly, a spreading droplet tends to adhere to a hydrophilic surface while a hydrophobic surface tends to repel the spreading motion of the droplet.

In Fig. 14, the influence of the drop inertia on the spreading of the lamella is shown, keeping the Weber number at a constant value of

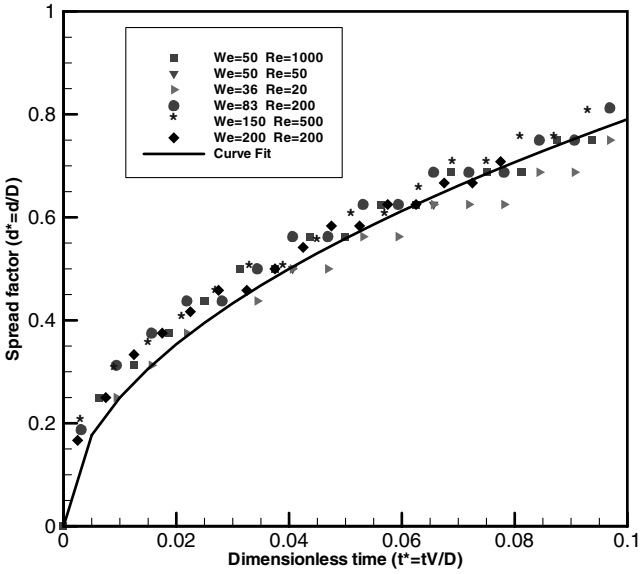

Fig. 10 Time evolution of spread factor during kinematic phase at various Weber and Reynolds numbers; the sold line is the curve fit $d/D = 2.5t^{*0.5}$.

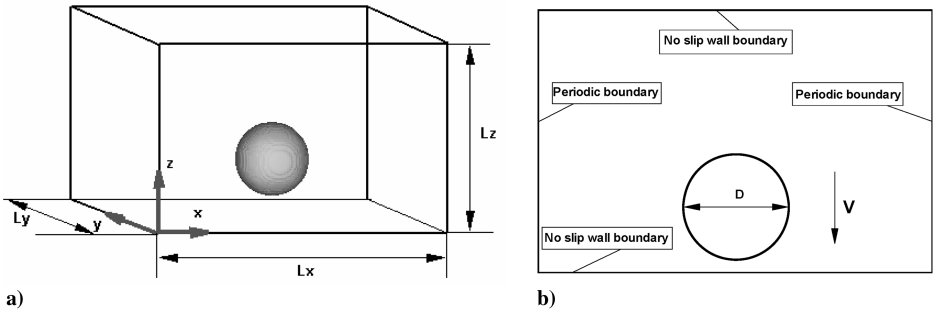

Fig. 7 Schematic of simulation domain for a droplet impingement on a dry surface.

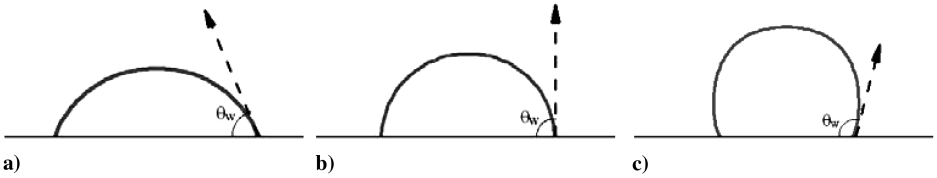

Fig. 8 Preliminary wetting tests for three surfaces: hydrophilic, neutral, and hydrophobic.

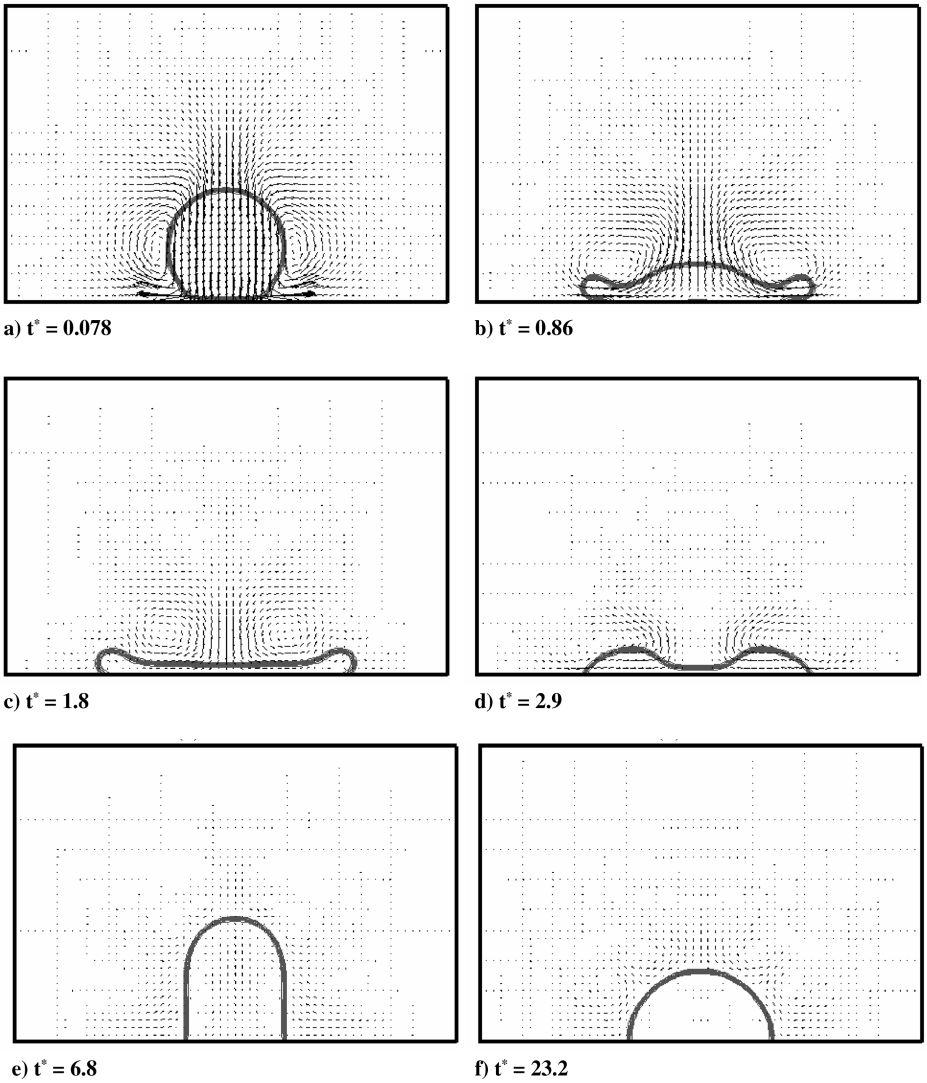

Fig. 11 Time evolution of droplet shape for $We = 50$, $Re = 1000$.

36. Evidently, an increase in the Reynolds number leads to an increase in the maximum spread factor. At $Re = 20$, the maximum value for d^* is 1.5; at $Re = 100$, $d^*_{\max} = 2.0$; at $Re = 200$, $d^*_{\max} = 2.1$. From $Re = 20$ to $Re = 100$, the maximum spread factor increases by 33%, while from $Re = 100$ to $Re = 200$, the maximum spread factor only increases by 5%.

In Fig. 15, the influence of the surface tension on the spreading process is compared by varying the Weber number while keeping the Reynolds number fixed at 200. As reported in an earlier study [23], the influence of the Weber number is weak, as can be seen from Fig. 15. At $We = 36$, $d^*_{\max} = 2.1$; at $We = 83$, $d^*_{\max} = 2.2$.

G. Splashing Breakup

In general, there are two possible outcomes of a droplet impingement on a solid dry surface, namely, deposition and splashing. Splashing is considered to be a more energetic pattern of impact outcome compared to deposition, as secondary droplets are ejected. Several experimental correlations have been proposed to quantify the deposition-splashing boundary. However, none of them have been proven to be universal [25].

One important and easier starting point to solve this problem is by the principle of mass and energy conservation before and after the impact [26]:

$$E_k + E_p + E_s = E'_k + E'_p + E'_s + E'_d, \qquad m = m' \tag{39}$$

where E_k, E_p, E_s, and E_d are the kinetic, potential, surface, dissipated energies, respectively, and m and m' is the mass of the droplet before and after impact.

Thus, if $E_k + E_p + E_s > E'_k + E'_p + E'_s + E'_d$, it indicates that the energy before impact is not completely dissipated by the surface tension and viscous forces. This can lead to the formation of secondary droplets and splashing may occur.

The kinetic energy before impact can be written as

$$E_k = \tfrac{1}{12}\rho_L V^2 \pi D^3 \tag{40}$$

The surface energy before impact can be written as

$$E_s = \pi D \sigma \tag{41}$$

The surface energy after impact can be written as

$$E'_s = \frac{\pi}{4} d^2_{\max} \sigma (1 - \cos\theta) \tag{42}$$

where θ is the contact angle between the liquid–gas interface and the solid when the lamella reached its maximum spreading diameter.

It is difficult to determine the dissipated energy because the velocity distribution inside the deforming droplet is not known. Chandra and Avedisian [27] used a very simple approximation to determine E'_d:

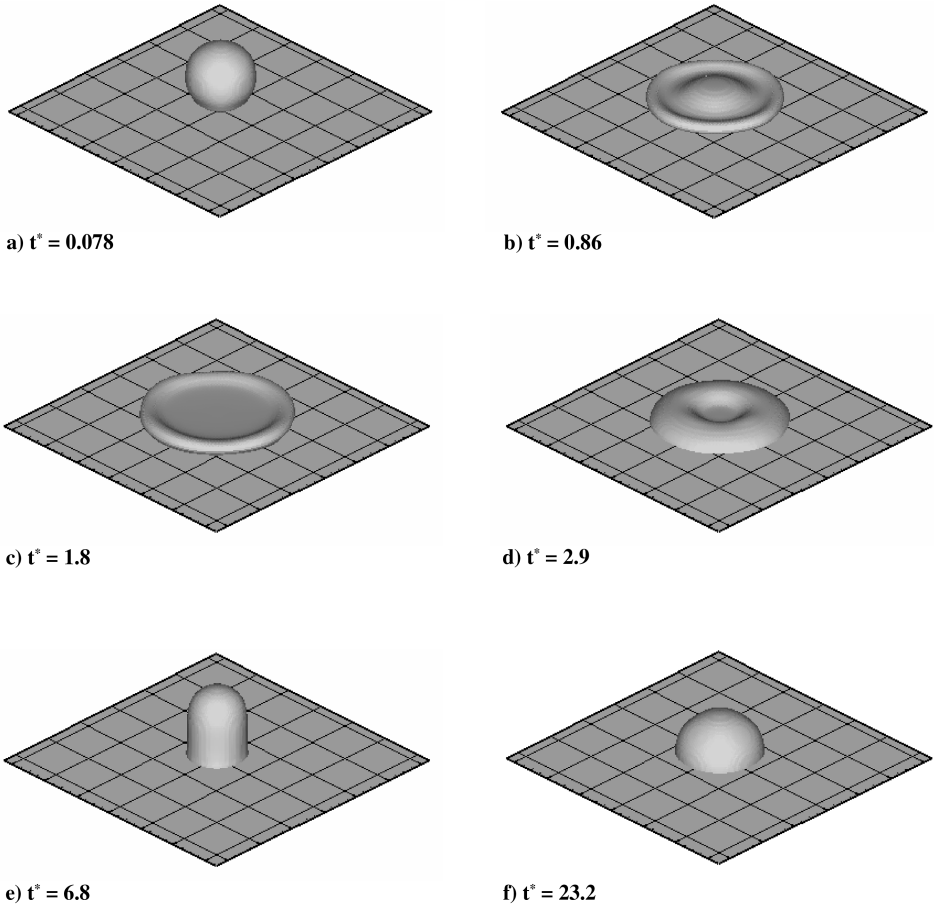

Fig. 12 Three-dimensional snapshots to show the time evolution of the droplet shape.

$$E'_d = \int_0^{t_d} \int_v \Phi^* \mathrm{d}v^* \mathrm{d}t \approx \Phi^* v^* t_d \tag{43}$$

where Φ is the dissipation per unit mass, and is given by

$$\Phi = \mu\left(\frac{\partial u_x}{\partial y} + \frac{\partial u_y}{\partial x}\right)\frac{\partial u_x}{\partial y} \approx \mu\left(\frac{V}{h}\right)^2 \tag{44}$$

t_d is the time it takes for the drop to deform to a maximum, which is approximated by $t_d = D/V$. v is the volume of the lamella and is given by $v \approx (\pi/4)d_{\max}^2 h$.

Combining Eqs. (39–44), and assuming $E_p = E'_p$, we obtain a reduced form of Eq. (39) in terms of Weber number, Reynolds number, and the maximum dimensionless spread factor,

$$\frac{3}{2}\frac{We}{Re}(d^*_{\max})^2 + (1-\cos\theta)(d^*_{\max})^2 - \left(\frac{1}{3}We + 4\right) = 0 \tag{45}$$

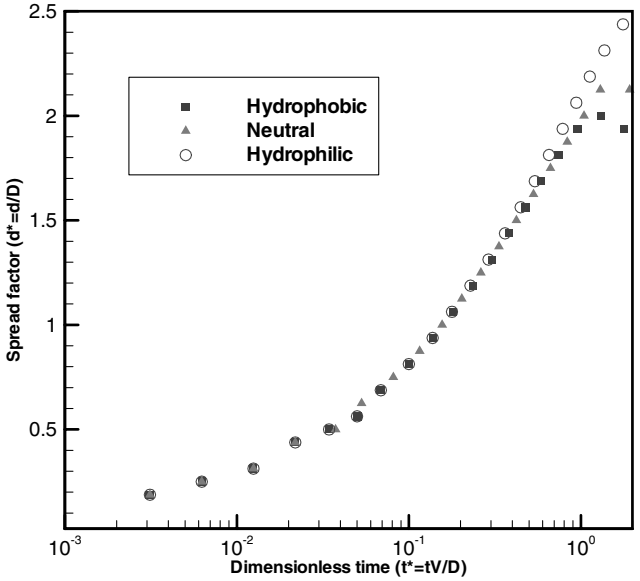

Fig. 13 Wettability influence on the spreading behavior during the spreading phase. ($We = 50$, $Oh = 0.0071$).

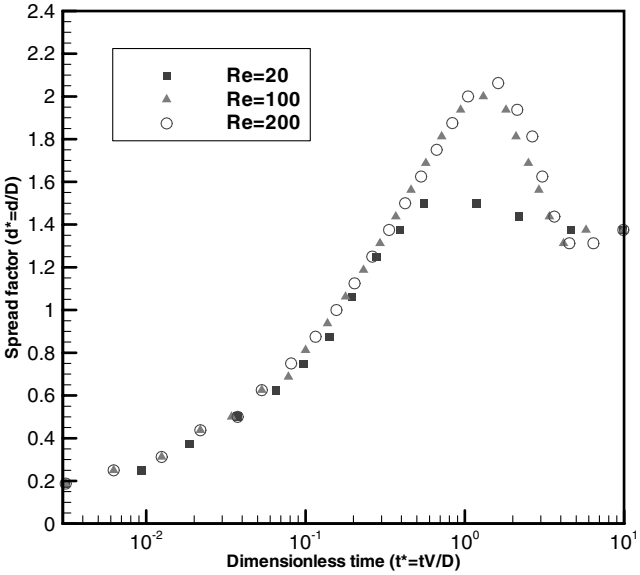

Fig. 14 Reynolds number influence on the spreading behavior during the spreading phase ($We = 36$ for all three cases).

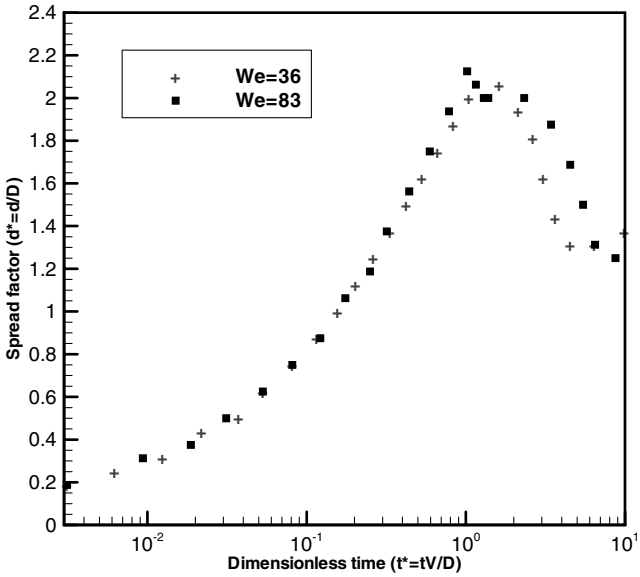

Fig. 15 Weber number influence on the spreading behavior during the spreading phase ($Re = 200$ for both cases).

This could also be written in terms of Ohnesorge number as

$$Oh_c = \sqrt{\frac{3(1-\cos\theta)(d^*_{\max})^2 - 12}{Re^2 - 4.5(d^*_{\max})^4 Re}} \tag{46}$$

Equation (46) determines the deposition-splashing boundary in terms of the Ohnesorge number and Reynolds number. However, this theoretical analysis based on simplifying assumptions may not be accurate enough to quantify the deposition-splashing boundary. At the same time, an analysis of this kind could qualitatively show the effect of increasing the Reynolds and Weber numbers and their influence on splashing.

In Fig. 16, two simulation results in the plane of $y = L_y/2$ are shown to compare deposition with splashing at the same Reynolds number of 200, but at different Ohnesorge numbers, $Oh = 0.03$, $Oh = 0.046$, respectively. The dynamic behavior of the droplets at different t^* is given side by side for the two different Ohnesorge numbers. In Fig. 17, the three-dimensional droplet impact outcomes are shown as a function of time for the splashing case. Assuming the same θ for both cases, with $d^*_{\max} = 2.2$, the maximum value of the critical Ohnesorge number is $Oh_c \approx 0.03$. For $Oh = 0.046$, the droplet will splash according to the theoretical analysis; whereas for $Oh = 0.03$, it is difficult to determine whether splashing will occur or not. However, according to the experimental correlation proposed by several authors [4,26], the demarcation between deposition and spreading of droplets can be determined based on the value of K', where $K' = We * Oh^{-0.4} = 650$ is the proposed deposition/splash threshold. For $We = 36$, $K' = 146.4$ and according to this correlation, it will not splash as also seen in our LBM simulation. For $We = 83$, $K' = 285.5$, the deposition/splash threshold is not exceeded and therefore no splash can be expected. However, as already seen in the LBM simulation and the theoretical prediction, this case for $K' = 285.5$ does result in a splash. A qualitative comparison of the two outcomes (dotted region shown in Fig. 16) at $t^* = 1.41$ illustrates the deposition-splashing boundary, and is shown in Fig. 18. This disagreement in the experimental and current simulation questions the accuracy of the proposed correlation [4,26].

However, there are two major differences in the present numerical modeling of splash and the experiments on which the above-mentioned correlation is based. First, the density ratio of the liquid droplet and surrounding gas phase is fixed at 50 for the current simulations. This value is relatively small compared to the experimental data, which is in the range of 1000 for an air–water system at atmospheric pressure. This difference in density ratio translates to different values of the relative pressure between the simulations and experiments, with the relative pressure of the surrounding medium to be higher in the present LBM simulations as compared to that of experiments. No experiments have ever been reported regarding the influence of the ambient pressure on splashing, except one surprising discovery recently brought forward by Xu et al. [28]. They experimentally investigated the effect of the ambient pressure or the molecular weight of the surrounding gas on the splashing of droplets. Corona splash was the outcome when an alcohol drop was allowed to impinge on a dry surface at atmospheric pressure. However, when the pressure was reduced by a factor of 5, the corona completely disappeared and no splashing was observed. Thus, the relative density (or pressure) of the surrounding gas may have a large influence on the deposition-splashing boundary and may be the cause of the discrepancy in the threshold set by the correlation. Current simulations, shown for a relative density ratio of 50, indicate that splashing might have been achieved as a consequence of the higher surrounding pressure of the ambient gas, and hence does not match with the existing experimental correlation which was proposed for a liquid–gas system of relative density of 1000. Clearly, a mechanism of this kind of influence on the final outcome warrants further study. Secondly, the surface roughness and the uncertainty in the experiments are also factors in splashing. These factors were not reproduced due to the nature of the current LBM simulations, because the surface of impact is considered to be ideally smooth and the simulation conditions are isotropic.

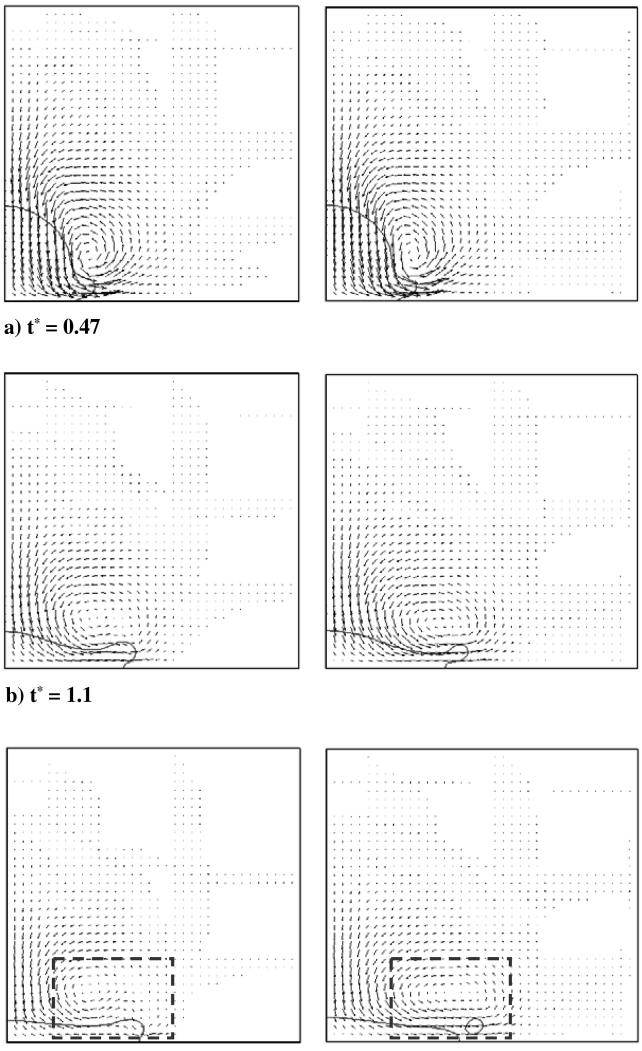

Fig. 16 Comparison between deposition and splashing breakup ($We = 36$ on the left for $Oh = 0.03$ and $We = 83$ on the right for $Oh = 0.046$, both at $Re = 200$).

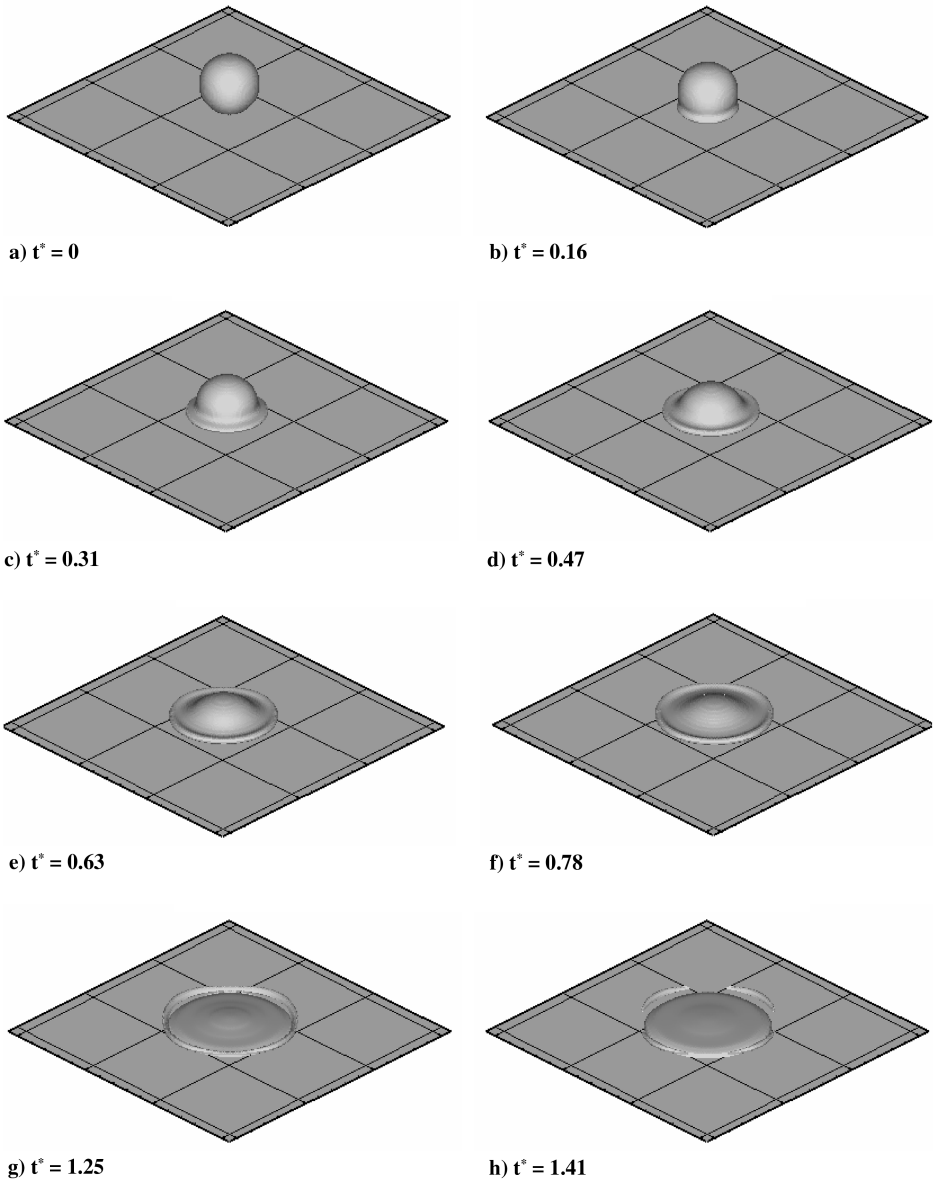

Fig. 17 Three-dimensional simulation results to show splashing breakup after the droplet reaches its maximum spread factor ($We = 83$, $Oh = 0.046$).

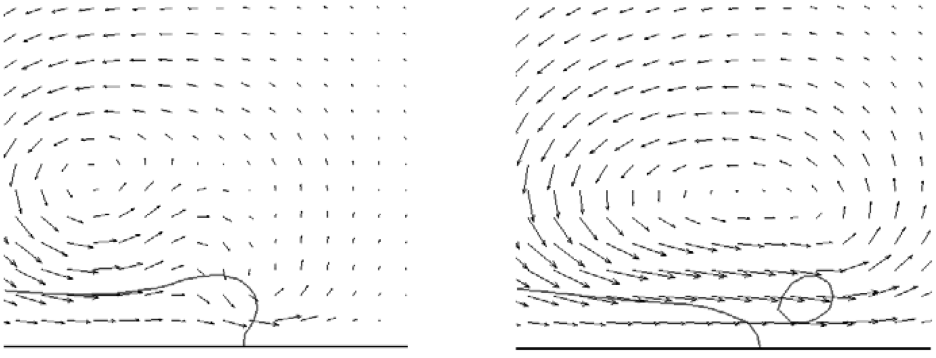

Fig. 18 Zoomed-in comparison between deposition and splashing breakup [same as c) in Fig. 16].

V. Conclusions

In this work, a lattice Boltzmann method is presented to simulate droplet collision and droplet impact at a relatively large density ratio of 50 in a three-dimensional Cartesian system. The current method has its benefits, considering the numerical instability which arises when dealing with large density ratios in LBM [10–13]. The surface wettability is suitably incorporated by a novel boundary treatment. Hydrophilic, neutral, and hydrophobic surfaces have been successfully simulated to study the role of surface wetting characteristics in droplet impingement problems. Simulations of binary droplet collisions are primarily conducted to validate the methodology for $20 < We < 80$. Three different types of outcome, namely, coalescence collision, separating collision, and stretching collision, have been presented.

It is shown that during the early stage of impact, the spread factor is proportional to a power of dimensionless time, given by $d^*_{max} = 2.5t^{*0.5}$. It compares well with the theoretical analysis and existing experimental correlations [23]. In the spreading phase, it is shown that the maximum spread factor increases with an increase in Reynolds number and Weber number, where Reynolds number is found to have a higher influence. In addition, maximum spread factors are found to increase in the ascending order when comparing hydrophobic, neutral, and hydrophilic surfaces.

Two different outcomes of impingement have been shown: deposition and splashing. Splashing occurs at a higher Reynolds number and Ohnesorge number compared to deposition. The transition to splashing is qualitatively studied by simple energy analysis. Because the density or pressure of the surrounding gas phase also plays a key role in determining the deposition-splashing threshold, it is shown that the threshold obtained in the presented simulation results is lower than the experimental data. Although the effect of pressure needs further study, it appears that splashing can be avoided by reducing the system pressure.

Future study is directed toward the quantification of deposition/splashing threshold at a higher density ratio of order 1000. In addition, simulations at different density ratios are needed to compare the influence of the surrounding gas phase on the impingement outcomes.

References

[1] Yarin, A. L., "Drop Impact Dynamics: Splashing, Spreading, Receding, Bouncing. . .," *Annual Review of Fluid Mechanics*, Vol. 38, Jan. 2006, pp. 159–192. doi:10.1146/annurev.fluid.38.050304.092144

[2] Wachters, L. H. J., and Westerling, N. A. J., "The Heat Transfer from a Hot Wall to Impinging Water Drops in the Spheroidal State," *Chemical Engineering Science*, Vol. 21, No. 11, Nov. 1966, pp. 1047–1056. doi:10.1016/0009-2509(66)85100-X

[3] Stow, C. D., and Hadfield, M. G., "An Experimental Investigation of Fluid Flow Resulting from the Impact of a Water Drop with an Unyielding Dry Surface," *Proceedings of the Royal Society of London A*, Vol. 373, No. 1755, Jan. 1981, pp. 419–441. doi:10.1098/rspa.1981.0002

[4] Cossali, G. E., Coghe, A., and Marengo, M., "The Impact of a Single Drop on a Wetted Solid Surface," *Experiments in Fluids*, Vol. 22, No. 6, 1997, pp. 463–472. doi:10.1007/s003480050073

[5] Morton, D., Rudman, M., and Jong-Leng, L., "An Investigation of the Flow Regimes Resulting from Splashing Drops," *Physics of Fluids*, Vol. 12, No. 4, April 2000, pp. 747–763. doi:10.1063/1.870332

[6] Josserand, C., and Zaleski, S., "Droplet Splashing on a Thin Liquid Film," *Physics of Fluids*, Vol. 15, No. 6, May 2003, pp. 1650–1657. doi:10.1063/1.1572815

[7] Mukherjee, S., and Abraham, J., "Lattice Boltzmann Simulations of Two-Phase Flow with High Density Ratio in Axially Symmetric Geometry," *Physical Review E*, Vol. 75, No. 2, Feb. 2007, pp. 026701.1–026701.13.

[8] Mukherjee, S., and Abraham, J., "Crown Behavior in Drop Impact on Wet Walls," *Physics of Fluids*, Vol. 19, No. 5, May 2007, pp 052103.1–052103.10.

[9] Lee, T., and Lin, C.-L., "A Stable Discretization of the Lattice Boltzmann Equation for Simulation of Incompressible Two-Phase Flows at High Density Ratio," *Journal of Computational Physics*, Vol. 206, No. 1, June 2005, pp. 16–47. doi:10.1016/j.jcp.2004.12.001.

[10] Gunstensen, A. K., Rothman, D. H., Zaleski, S., and Zanetti, G., "Lattice Boltzmann Model of Immiscible Fluids," *Physical Review A*, Vol. 43, No. 8, April 1991, pp. 4320–4327. doi:10.1103/PhysRevA.43.4320

[11] Shan, X., and Chen, H., "Lattice Boltzmann Model for Simulating Flows with Multiple Phases and Components," *Physical Review E*, Vol. 47, No. 3, March 1993, pp. 1815–1819. doi:10.1103/PhysRevE.47.1815

[12] Swift, M. R., Osborn, W. R., and Yeomans, J. M., "Lattice Boltzmann Simulation of Nonideal Fluids," *Physical Review Letters*, Vol. 75, No. 5, July 1995, pp. 830–833. doi:10.1103/PhysRevLett.75.830

[13] He, X., Chen, S., and Zhang, R., "A Lattice Boltzmann Scheme for Incompressible Multiphase Flow and its Application in Simulation of Rayleigh-Taylor Instability," *Journal of Computational Physics*, Vol. 152, No. 2, July 1999, pp. 642–663. doi:10.1006/jcph.1999.6257

[14] Inamuro, T., Ogata, T., Tajima, S., and Konishi, N., "A Lattice Boltzmann Method for Incompressible Two-Phase Flows with Large Density Differences," *Journal of Computational Physics* Vol. 198, No. 2, Aug. 2004, pp. 628–644. doi:10.1016/j.jcp.2004.01.019

[15] Briant, A. J., Wagner, A. J., and Yeomans, J. M., "Lattice Boltzmann Simulations of Contact Line Motion. I. Liquid-Gas System," *Physical Review E*, Vol. 69, No. 3, March 2004, pp. 031602–031616. doi:10.1103/PhysRevE.69.031602

[16] Mo, G. C. H., Liu, W., and Kwok, D. Y., "Surface-Ascension of Discrete Liquid Drops via Experimental Reactive Wetting and Lattice Boltzmann Simulation," *Langmuir*, Vol. 21, No. 13, 2005, pp. 5777–5782. doi:10.1021/la0472854

[17] Kang, Q., Zhang, D. S., and Chen, J., "Displacement of a Three-Dimensional Immiscible Droplet in a Duct," *Fluid Mechanics*, Vol. 545, Dec. 2005, pp. 41–66. doi:10.1017/S0022112005006956

[18] Benzi, R., Biferale, L., Sbragaglia, M., Succi, S., and Toschi, F., "Mesoscopic Modeling of a Two-Phase Flow in the Presence of Boundaries: The Contact Angle," *Physical Review E*, Vol. 74, No. 2, Aug. 2006, pp 021509.1–021509.14.

[19] Lee, T., and Liu, L., "Wall Boundary Conditions in the Lattice Boltzmann Equation Method for Nonideal Gases," *Physical Review E*, Vol. 78, July 2008, pp 017702.1–017702.4.

[20] Mukherjee, S., and Abraham, J., "Investigations of Drop Impact on Dry Walls with a Lattice-Boltzmann Model," *Journal of Colloid and Interface Science*, Vol. 312, No. 2, Aug. 2007, pp. 341–354. doi:10.1016/j.jcis.2007.03.004

[21] Gupta, A., and Kumar, R., "Simulation of Droplet Flows Using Lattice Boltzmann Method," *Proceedings of the Sixth International ASME Conference on Nanochannels, Microchannels and Minichannels*, American Society of Mechanical Engineers, New York, June 2008.

[22] Cahn, J. W., "Critical Point Wetting," *Journal of Chemical Physics*, Vol. 66, No. 8, April 1977, pp. 3667–3672. doi:10.1063/1.434402

[23] Rioboo, R., Marengo, M., and Tropea, C., "Time Evolution of Liquid Drop Impact onto Solid, Dry Surfaces," *Experiments in Fluids*, Vol. 33, No. 1, 2002, pp. 112–124.

[24] Zheng, H. W., Shu, C., and Chew, Y. T., "A Lattice Boltzmann Model for Multiphase Flows with Large Density Ratio," *Journal of Computational Physics*, Vol. 218, No. 1, 2006, pp. 353–371. doi:10.1016/j.jcp.2006.02.015

[25] Bussmann, M., Chandra, S., and Mostaghimi, J., "Modeling the Splash of a Droplet Impacting a Solid Surface," *Physics of Fluids*, Vol. 12, No. 12, Dec. 2000, pp. 3121–3132. doi:10.1063/1.1321258

[26] Mundo, C. H. R., Sommerfeld, M., and Tropea, C., "Droplet-Wall Collisions: Experimental Studies of the Deformation and Breakup Process," *International Journal of Multiphase Flow*, Vol. 21, No. 2, 1995, pp. 151–173. doi:10.1016/0301-9322(94)00069-V

[27] Chandra, S., and Avedisian, C. T., "On the Collision of Droplet with a Sold Surface," *Proceedings of the Royal Society of London A*, Vol. 432, No. 1884, 1991, pp. 13–41. doi:10.1098/rspa.1991.0002

[28] Xu, L., Zhang, W. W., and Nagel, S. R., "Drop Splashing on a Dry Smooth Surface," *Physical Review Letters*, Vol. 94, No. 18, 2005, pp 184505.1–184505.4.